Thermo X
https://doi.org/10.70401/tx.2026.0025

Supplementary information

Reconfigurable solid-state thermal routing using thermoelectric effects

Ran Ju, Yanxiang Wang, Zifu Xu, Kaile Sun, Shuihua Yang, Dong Wang, Minghong Qi, Pei-Chao Cao, Hongsheng Chen, Cheng-Wei Qiu, Ying Li

Section S1: Fitting of the Seebeck coefficient and theoretical analysis of single thermoelectric slab.

Section S2: Seebeck coefficient-temperature diagram of the backward working process.

Section S3: The theoretical model of the thermal router.

Section S4: Derivation of the formula for the heat absorbed by the drain.

Section S5: Analysis regarding energy efficiency.

Section S6: Component extraction method for the demonstration of Thomson contribution.

Section S7: The calculation of effective Seebeck coefficient S_{eff}.

Section S8: Method of calculating heat flux from temperature data.

Section S9: Discussion of the discrepancy in split ratios between ideal and experimental cases.

Section S10: The dependence of thermal splitting performance on the router's geometrical size.

Section S11: Experimental design, statistical analysis, and model parameters.

Section S1: Fitting of the Seebeck coefficient and theoretical analysis of single thermoelectric slab

Thermoelectric effects have attracted renewed research interest since the early 21st century due to the discovery of high-performance TE materials. The three most commonly employed longitudinal TE effects are the Seebeck effect, the Peltier effect, and the Thomson effect. Seebeck effect describes the generation of thermoelectric potential in a material with a temperature difference on it. On the contrary, Peltier effect arises when an electric current passes through the interface between two materials with different Seebeck coefficients, resulting in either heat absorption or release at the junction. The associated heat power can be expressed as $q=JST$, where J, S and T are the electric current density, Seebeck coefficient, and temperature, respectively. This relation establishes a direct proportionality between the Seebeck coefficient S and the Peltier heat power q. Strictly speaking, the Peltier effect is an interfacial phenomenon, occurring only at junctions between dissimilar materials. However, Thomson revealed that heat generation or absorption can also occur within a homogeneous material under a thermal gradient when an external electric current is applied. Such a distributed Peltier effect, or Thomson effect, arises from the temperature dependence of the Seebeck coefficient, with the Thomson coefficient defined as $\tau=T\frac{dS}{dT}$.

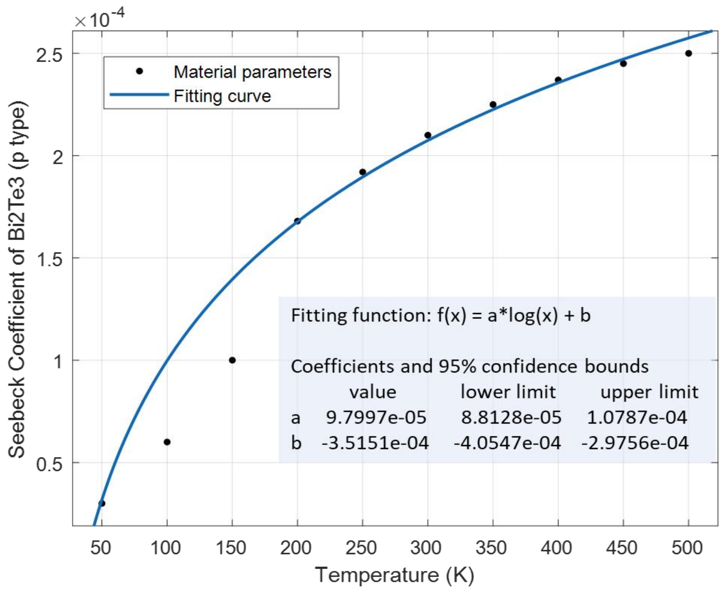

Figure S1. The fitting curve and estimated parameters of the fitting function.

The Seebeck and Peltier effects are thermodynamically inverse phenomena describing the mutual conversion between thermal and electrical energy, while the Thomson effect unifies these two under the first law of thermodynamics. To be noted, the Thomson coefficient $\tau=T\frac{dS}{dT}$ is a function of temperature T, which introduces nonlinearity in the heat diffusion equation and prevents the obtainment of an analytical solution to the temperature distribution. Through an inspection of the temperature dependence of Seebeck coefficient S, it can be found that a logarithmic function is satisfied between T and S. Therefore, by setting $S=\tau\mathrm{In}(T)+b$, we can bypass the problem of nonlinearity and enable the acquisition of an analytical general solution to Eq. (1) in the main text.

Substituting the temperature-dependent Seebeck coefficient of Bi_2Te_3 into MATLAB and fitting these data, we can get the following fitting curve and parameter values, shown in Figure S1. According to the fitting result, here we consider the Thomson coefficient τ to be 9.8×10^{-5} V/K in the following calculation of mathematic model. The governing equation for steady-state one dimensional macroscopic heat diffusion considering both thermoelectric effects and Joule effect is given as:

$$\kappa\frac{d^2T}{dx^2}\text{-}J\tau\frac{dT}{dx}+\frac{J^2}{\sigma}=0 \tag{S1}$$

The general solution of this equation is $T(x)=C_1+C_2e^{\frac{J\tau}{\kappa}x}+\frac{J}{\tau\sigma}x$, where C_1 and C_2 are undetermined coefficients which depend on the boundary conditions. In our model, both ends of the TE leg are maintained at fixed temperatures: a heat source at high temperature T_1 and a heat sink at low temperature T_2. Accordingly, by applying the Dirichlet boundary condition $T(x=0)=T_1$ and $T(x=L)=T_2$, the expression of C_1 and C_2 can be confirmed, where $C_1=\frac{T_1e^{\frac{J\tau}{\kappa}L}\text{-}T_2+nL}{e^{\frac{J\tau}{\kappa}L}\text{-}1}$ and $C_2=\frac{T_2\text{-}T_1\text{-}nL}{e^{\frac{J\tau}{\kappa}L}\text{-}1}$.

Besides, under the condition where Thomson effect is ignored, namely, Seebeck coefficient is independent on temperature ($\tau=T\frac{dS}{dT}=0$), the governing equation above will degenerate into the form $\kappa\frac{d^2T}{dx^2}+\frac{J^2}{\sigma}=0$, and the according general solution of this equation is a parabolic curve $T(x)=\text{-}\frac{J^2}{2\sigma\kappa}x^2+C_2x+C_1$. Likewise, by applying the constant temperature boundary conditions $T(x=0)=T_1$ and $T(x=L)=T_2$, the expression of C_1 and C_2 can be determined as $C_1=T_1$ and $C_2=(T_2\text{-}T_1+\frac{J^2L^2}{2\sigma\kappa})/L$. For heat diffusion mediated by thermoelectric effects, the formula of heat flux is $q=\text{-}\kappa\frac{dT}{dx}+JST$. Substitute the expression of temperature distribution above into this formula, the heat flux flowing into the targeted port can be determined.

Section S2: Seebeck coefficient-temperature diagram of the backward working process

The structure setup of the backward case is shown in Figure S2a. Compared with the forward case, the direction of electric current remains the same, while the positions of the heat source and drain are switched. By doing so, the working mode of Thomson effect in the device is reversed, as directly revealed by the S-T diagram shown in Figure S2b and Figure S2c.

In the backward case, the working path in the S-T diagram transforms from the counter-clockwise mode to the clockwise mode. This diagram of comprises four processes: (D→C) current is driven by the external circuit from the hot end to cold end of the rectifier; (C→B) at the cold end, heat is absorbed as current enters the TE slab, increasing S from S_0 to S_{av}; (B→A) current flows through the TE slab from cold to hot, transporting heat; and finally (A→D) heat is released as current leaves the TE slab at the hot end, closing the cycle. In these diagrams, regions shaded in warm colors denote heat released, while those in cool colors represent heat absorbed.

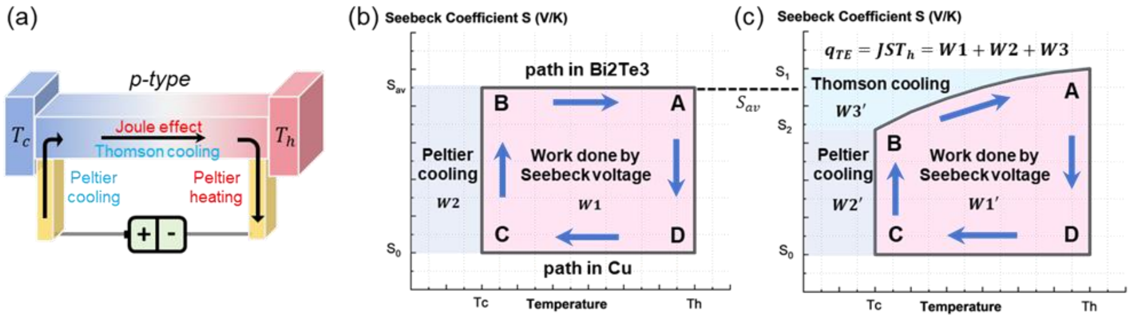

Figure S2. (a) The forward case of the single slab thermal rectifier. (b-c) The S-T diagram of the backward working process in the thermal rectification device with a constant (b) or a temperature-dependent (c) Seebeck coefficient.

To be noted, when considering the Thomson effect shown in Figure S2c, the work *W3* labeled by the blue region does not contribute directly to the heat absorbed or released at the drain port. Instead, it converts the latent heat into temperature first, and then affects the drain port through thermal conduction. Interestingly, the conversion rate is closely related to the working electric current applied. Therefore, when considering whether Thomson effect will lead to an enhancement in the rectification performance compared with the case where a constant Seebeck coefficient is employed, a phase figure is needed, as shown in the inner Figure 2d of the main text.

Section S3: The theoretical model of the thermal router

The governing equation for one dimensional heat transfer considering thermoelectric effects and heat exchange with surrounding environment is given as:

$$\kappa\frac{d^2T}{dx^2}\text{-}J\tau\frac{dT}{dx}+\frac{J^2}{\sigma}+\mathrm{h}(T_0\text{-}T)=0 \tag{S2}$$

where h is the heat exchange coefficient and T_0 is the surrounding temperature. The general solution is:

$$T(x)=Ce^{\frac{\frac{J\tau}{\kappa}+\sqrt{\left(\frac{J\tau}{\kappa}\right)^2+\frac{4\mathrm{h}}{\kappa}}}{2}x}+De^{\frac{\frac{J\tau}{\kappa}-\sqrt{\left(\frac{J\tau}{\kappa}\right)^2+\frac{4\mathrm{h}}{\kappa}}}{2}x}+T_0+\frac{J^2}{\sigma\mathrm{h}} \tag{S3}$$

The structure of the model is shown in Figure S3a , based on which we can give the segmental governing equations of this structure according to the materials and physical process. For subregions exchanging heat with external reservoirs (subregions 1,3,5, with length L_1), the material is copper, and the surrounding temperature is the temperature of external reservoirs attached to the source or drain port, denoted as T_{h} or T_c. Furthermore, considering that these exists no bulk thermoelectric effect (τ=0) in copper, the governing equations for these subregions are:

$$T_{1,3,5}(\mathrm{x})=C_{1,3,5}e^{\sqrt{\frac{\mathrm{h}_1}{k}}x}+D_{1,3,5}e^{-\sqrt{\frac{\mathrm{h}_1}{k}}x}+T_{\mathrm{h}/c}+\frac{J^2}{\sigma\mathrm{h}_1} \tag{S4}$$

where h_1 is the heat transfer coefficient between the external reservoir and subregions 1, 3, and 5.

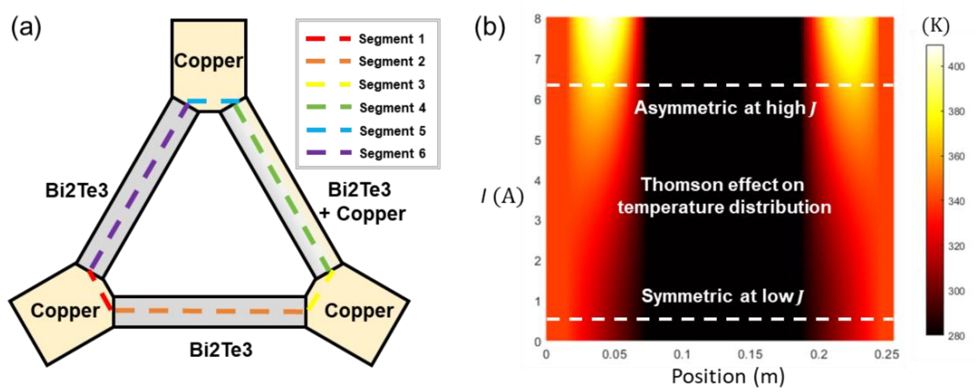

Figure S3. (a) The structure of the diffusive thermal router. (b) The temperature of the thermal router as a function of both the position and electric current *I*.

For subregions 2,4,6 (with length L_2), the materials are either Bi_2Te_3 or the composite structure composed of both Bi_2Te_3 and copper, so Thomson effect must be considered ($\tau\neq0$). Besides, since the thermal conductivity of Bi_2Te_3 is very low, the heat exchanging between these sections and the environment through natural convection is substantial. Therefore, the governing equations for these subregions are:

$$T_{2,4,6}(x)=C_{2,4,6}e^{\frac{\frac{J\tau}{\kappa}+\sqrt{\left(\frac{J\tau}{\kappa}\right)^2+\frac{4\mathrm{h}_2}{\kappa}}}{2}x}+D_{2,4,6}e^{\frac{\frac{J\tau}{\kappa}-\sqrt{\left(\frac{J\tau}{\kappa}\right)^2+\frac{4\mathrm{h}_2}{\kappa}}}{2}x}+T_e+\frac{J^2}{\sigma\mathrm{h}_2} \tag{S5}$$

where h_2 is the heat transfer coefficient between channels and environment, T_e is the temperature of environment. By setting h_2 to be zero, Eq. S5 will degenerate to the case where natural convection between TE channels and air is ignored, like that in a vacuum space.

Based on the discussion above, one can obtain the simplified equations as follows:

$$\begin{cases} T_{1,3,5}(x)=C_i e^{m_i x}+D_i e^{n_i x}+T_{h/c}+u_i \\ T_{2,4,6}(x)=C_i e^{m_i x}+D_i e^{n_i x}+T_e+u_i \end{cases} \tag{S6}$$

To describe the physical properties of each segment precisely, variables m_i, n_i and $u_i$must be set according to the parameters of real constituent materials, as shown below

$$m_i=\begin{cases} \sqrt{h_1/\kappa_{Cu}},\ i=1,3,5 \\ \dfrac{\dfrac{J\tau_{TE}}{\kappa_{TE}}+\sqrt{\left(\dfrac{J\tau_{TE}}{\kappa_{TE}}\right)^2+\dfrac{4h_2}{\kappa_{TE}}}}{2},\ i=2,6 \\ \dfrac{\dfrac{J\tau_{eff}}{\kappa_{eff}}+\sqrt{\left(\dfrac{J\tau_{eff}}{\kappa_{eff}}\right)^2+\dfrac{4h_2}{\kappa_{eff}}}}{2},\ i=4 \end{cases};n_i=\begin{cases} -\sqrt{\dfrac{h_1}{\kappa_{Cu}}},\ i=1,3,5 \\ \dfrac{\dfrac{J\tau_{TE}}{\kappa_{TE}}-\sqrt{\left(\dfrac{J\tau_{TE}}{\kappa_{TE}}\right)^2+\dfrac{4h_2}{\kappa_{TE}}}}{2},\ i=2,6 \\ \dfrac{\dfrac{J\tau_{eff}}{\kappa_{eff}}-\sqrt{\left(\dfrac{J\tau_{eff}}{\kappa_{eff}}\right)^2+\dfrac{4h_2}{\kappa_{eff}}}}{2},\ i=4 \end{cases};u_i=\begin{cases} 0,\ i=1 \\ \dfrac{J^2}{\sigma_{Cu}h_1},\ i=3,5 \\ \dfrac{J^2}{\sigma_{TE}h_2},\ i=2,6 \\ \dfrac{J^2}{\sigma_{eff}h_2},\ i=4 \end{cases}$$

Here, τ_{TE} (τ_{eff}), κ_{TE} (κ_{eff}), and σ_{TE} (σ_{eff}) denote the Thomson coefficient, thermal conductivity, and electrical conductivity of Bi_2Te_3 and the composite material, respectively. The heat exchange rate h_1 here can be expressed as $h_1=\kappa_{Cu}/(x_0 w)$, where x_0 and w are length of the port and width of the heat exchanging subregion, respectively, while h_2 is an empirical parameter.

Unlike the previous single-slab model, the present system involves multiple complex interfaces and boundary conditions across different regions. Thus, a direct application of the previous simple model is insufficient. To obtain the temperature distribution, one has to give twelve matching conditions, six groups for temperature and other six groups for flux conservation. For clarity, here we divide these matching conditions into the following two groups.

- Temperature conditions:

$$\sum_{i=1}^{6}\left|T_i^{end}-T_{(i+1)\bmod 6}^{head}\right|=0 \tag{S7}$$

It means that the ending temperature of the i-th section equals the starting temperature of the $(i+1)$-th section.

- Energy conservation conditions:

$$\sum_{i=1}^{6}\left|\left[-\kappa_i\frac{dT_i^{end}}{dx}+J\alpha_i T_i^{end}\right]-\left[-\kappa_{(i+1)\bmod 6}\frac{dT_{(i+1)\bmod 6}^{head}}{dx}+J\alpha_{(i+1)\bmod 6}T_{(i+1)\bmod 6}^{head}\right]\right|=0 \tag{S8}$$

This set of conditions is given by the continuity of heat flux density at the interface, which considers both conduction contribution and thermoelectric contribution. According to the general solutions of temperature, the specific parameters can be substituted into the above equations, then one can obtain the following equations. To be noted, the length of section 1, 3, and 5 is L_1, while the length of section 2, 4, and 6 is L_2.

- Temperature conditions:

$$\begin{cases} C_1 e^{m_1(L_1)}+D_1 e^{n_1(L_1)}+u_1+T_{\mathrm{h}}=C_2+D_2+u_2+T_0 \\ C_3 e^{m_3(L_1)}+D_3 e^{n_3(L_1)}+u_3+T_c=C_4+D_4+u_4+T_0 \\ C_5 e^{m_5(L_1)}+D_5 e^{n_5(L_1)}+u_5+T_c=C_6+D_6+u_6+T_0 \end{cases} \tag{S9}$$

$$\begin{cases} \mathrm{C}_2 e^{m_2 L_2}+D_2 e^{n_2 L_2}+u_2+T_e=C_3+D_3+u_3+T_c \\ C_4 e^{m_4 L_2}+D_4 e^{n_4 L_2}+u_4+T_e=C_5+D_5+u_5+T_c \\ C_6 e^{m_6 L_2}+D_6 e^{n_6 L_2}+u_6+T_e=C_1+D_1+u_1+T_{\mathrm{h}} \end{cases} \tag{S10}$$

- Energy conservation conditions:

$$\begin{cases} -\kappa_1(C_1 m_1 e^{L_1 m_1}+D_1 n_1 e^{L_1 n_1})=-\kappa_2(C_2 m_2+D_2 n_2)+J(S_2-S_1)(C_2+D_2+u_2+T_e) \\ -\kappa_3(C_3 m_3 e^{L_1 m_3}+D_3 n_3 e^{L_1 n_3})=-\kappa_4(C_4 m_4+D_4 n_4)+J(S_4-S_3)(C_4+D_4+u_4+T_e) \\ -\kappa_5(C_5 m_5 e^{L_1 m_5}+D_5 n_5 e^{L_1 n_5})=-\kappa_6(C_6 m_6+D_6 n_6)+J(S_6-S_5)(C_6+D_6+u_6+T_e) \end{cases} \tag{S11}$$

$$\begin{cases} -\kappa_2(C_2 m_2 e^{m_2 L_2}+D_2 n_2 e^{L_2 n_2})=-\kappa_3(C_3 m_3+D_3 n_3)+J(S_3-S_2)(C_3+D_3+u_3+T_c) \\ -\kappa_4(C_4 m_4 e^{m_4 L_2}+D_4 n_4 e^{L_2 n_4})=-\kappa_5(C_5 m_5+D_5 n_5)+J(S_5-S_4)(C_5+D_5+u_5+T_c) \\ -\kappa_6(C_6 m_6 e^{m_6 L_2}+D_6 n_6 e^{L_2 n_6})=-\kappa_1(C_1 m_1+D_1 n_1)+J(S_1-S_6)(C_1+D_1+u_1+T_{\mathrm{h}}) \end{cases} \tag{S12}$$

Here, as stated previously, T_e, T_{h}, and T_c are the temperature of environment, temperature of the hot external reservoir and cold reservoir, respectively. Note that, Seebeck coefficient $S(T)$ of materials Bi_2Te_3 is a temperature-dependent variable rather than a constant. Therefore, although in the previous part an assumption has been done on the Thomson effect τ so that the governing differential equation can lead to an analytical general solution, the coupling equations here are no longer linear ones. As a result, an analytical solution for undetermined coefficients $C_{1\text{-}6}$ and $D_{1\text{-}6}$ can be extremely complicate if not impossible. Confronted with this hindrance, to solve this group of equations, we resort to Newton's method. It is a mature numerical optimization algorithm for nonlinear equations, and can lead to a precise solution at a relatively low cost.

To be mentioned, in the absence of an applied electric current, heat transport is driven solely by the temperature gradient between the source and the drains. Under such conditions, although majority carriers drift from the hot to the cold regions due to uneven kinetic energy distribution, they merely accumulate at the colder end rather than forming a circulating TE-induced shortcut electric current. This is because all thermoelectric components in our router are composed of the same carrier type, and no p-n junction exists in the system.

Section S4: Derivation of the formula for the heat absorbed by the drain

For the single TE slab model, the heat absorbed by the drain can be represented analytically by the simple formula $q=-\kappa\frac{dT}{dx}+JST$, since the heat flux flowing out of the TE leg exactly equals the quantity entering the drain, as shown in Figure S4b. However, for the thermal router, the heat energy absorbed by the drain cannot be described by such a simple relation. Focusing on this problem, we must analyze the part marked by the red dotted box in Figure S4a carefully.

As shown in Figure S4c, different from the configuration in Figure S4b, here the drain is sandwiched between two TE channels rather than connected with only one channel. Under this scenario, it is insufficient to consider only the heat flux entering the channel. Since electric current first flows into the drain then leaves the drain, so does the heat energy carried by electric current. According to the law of energy conservation, one can get the following relationship: $q^{\text{absorb}}=q^{\text{in}}-q^{\text{out}}+q_{\text{joule}}+W^{\text{TE}}$, where q^{in}, q^{out}, q_{joule}, and W^{TE} represent the heat inflow, heat outflow, heat generated by Joule effect, and the work done by the thermal-electromotive force in the drain or the work done to overcome the thermal-electromotive force. To be noted, W^{TE} can either be positive or negative, depending on the direction of external electric current and the inner electric field constructed by temperature gradient.

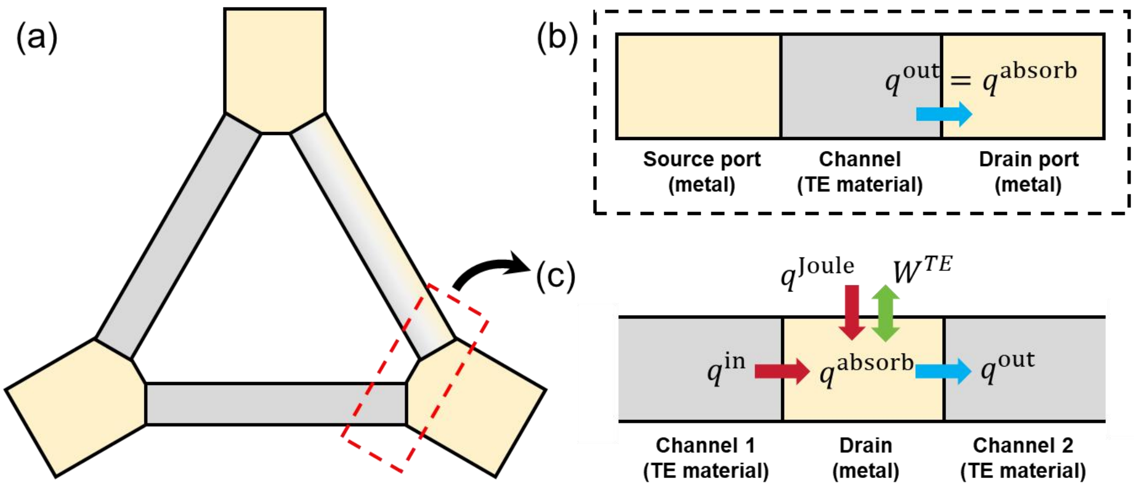

Figure S4. (a) The structure of thermal router. (b) The schematic of the heat absorbed by the single slab model. (c) The schematic of the heat energy absorbed by the drain of thermal router.

Therefore, the precise heat flux flowing from source to drain 1 and drain 2 are as follows:

$$\begin{cases} q_{\text{D1}}=q_{\text{D1}}^{\text{in}}-q_{\text{D1}}^{\text{out}}+q_{\text{joule}}+E_1J \\ q_{\text{D2}}=q_{\text{D2}}^{\text{in}}-q_{\text{D2}}^{\text{out}}+q_{\text{joule}}+E_2J \end{cases} \tag{S13}$$

where E_1 and E_2 are the inner electric field constructed by the temperature gradients in the subregion of drain 1 and drain 2, which can be calculated analytically through the formula $E=S\cdot\Delta T=-\frac{1}{e}\frac{\Delta\mu_e}{\Delta T}\Delta T=-\frac{\Delta\mu_e}{e}$.

What deserves a mention is that, since the material of the drain being used here is copper, with a weak Seebeck effect and a superb electric conductivity, even if the terms q_{joule} and E_1J are ignored, it will not cause a big difference to the thermal splitting effect of the thermal router. However, for the sake of rigor, we have still clarified the difference between this structure and the simple thermoelectric leg structure in the heat flux calculation method. Based on the consideration above, it is also acceptable for the heat flux flowing from source to drain 1 and drain 2 to be written in the following form:

$$\begin{cases} q_{\mathrm{D1}}=q_{\mathrm{D1}}^{\mathrm{in}}-q_{\mathrm{D1}}^{\mathrm{out}} \\ q_{\mathrm{D2}}=q_{\mathrm{D2}}^{\mathrm{in}}-q_{\mathrm{D2}}^{\mathrm{out}} \end{cases} \tag{S14}$$

Section S5: Analysis regarding energy efficiency

The split ratio is an important metric for the assessment of routing performance, however, it cannot fully characterize the practical performance of the device. To remedy this, here the electrical cost required for routing is analyzed. For this target, here we define a coefficient of performance as $COP=\frac{\Delta Q_{\mathrm{target}}}{P_{\mathrm{elec}}}=\frac{Q_{\mathrm{on}}\text{-}Q_{\mathrm{off}}}{P_{\mathrm{elec}}}$, where P_{elec} represents the electric power consumed, Q_{on} and Q_{off} represent the heat flux transferred to the target port when the electric current is applied or not. Through simulation, it can be found that COP is inversely proportional to electric current. This is understandable since the heat flux pumped by thermoelectric effects scales linearly with current, while electric power scales quadratically. However, COP can still reach 0.8 at the optimal working current I~3 A, which means that such an energy investment was worthwhile, since both unidirectionally heat transfer enhancement and isolation have been achieved.

Besides, what deserves a mention is that COP is a metric concerning the pumping performance rather than the efficiency of converting electrical energy into heat flux, for which it can be a quantity greater than one without violating the law of energy conservation.

Section S6: Component extraction method for the demonstration of Thomson contribution

To intuitively visualize the contribution of the Thomson effect to the temperature field on the thermal router, it is beneficial to separate its contribution from other effects. Notably, among the various mechanisms directly manifested as bulk temperature changes in this system, only Thomson effect exhibits an odd-parity response to the direction of electric current. Inspired by this physical principle, we try to extract the Thomson component from the overall temperature distribution, thereby directly revealing its role in asymmetric heat diffusion and the resulting thermal routing effect.

Traditionally, the well-known lock-in thermography (LIT) techniques combines periodic thermal excitation with time-sequenced thermal imaging to extract heat responses synchronized with the excitation frequency. In this approach, Fourier transform techniques are employed to separate ambient noise from the targeted signal. However, in the present study of the TE-enabled diffusive thermal router, we found that neither periodic thermal excitation nor time-sequenced thermography is necessary when the goal is specifically to extract the Thomson effect. As mentioned above, the Thomson effect uniquely exhibits a J-odd dependence. Leveraging this property, and noting that both positive and negative $J\nabla T$ terms coexist spatially within the device, we extract temperature data from pairs of symmetric points along the TE channel 1 and channel 3. Then, the J-odd-dependent thermoelectric signals can be obtained through the relation $T_{\mathrm{odd}}=[T(J)-T(-J)]/2$, so that the contributions from the temperature-gradient-driven conduction and Joule heating are eliminated.

It resembles that a square-wave electric current with an infinite period is applied, thus a pseudo-periodic temperature response at each point can be artificially constructed by using a spatial signal with odd symmetry to construct an equivalent time period. To minimize the disturbance of interfacial Peltier effect, the J-odd-dependent thermoelectric signals on the middle point of the Bi_2Te_3 slab are extracted for demonstration.

In additional to that, we have simulated three conditions of this device, namely, with all effects, with Seebeck and Joule effect, and with only Joule effect. Then, by normalizing the heat flux transferred to the targeting isolated port using the scenario without thermoelectric effects as the base, the respective contribution of Seebeck and Thomson effect can be revealed clearly.

Section S7: The calculation of effective Seebeck coefficient S_{eff}

For a better thermal split ratio of our device, the channel 2 of thermal router in this work is made by combing Bi_2Te_3 with copper, as shown in Figure S5. Herein, S_1 (S_2), σ_1 (σ_2), and C_1 (C_2) represent the Seebeck coefficients, electrical conductivities, and volume fractions of copper (Bi_2Te_3), respectively, with the constraint $c_1+c_2=1$.

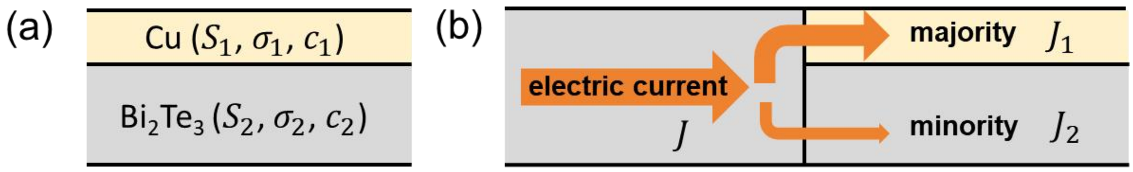

Figure S5. The schematic of the material composition of channel 2.

By weighting the individual Seebeck coefficients according to their respective electrical conductivities and volume fractions, the calculation of effective Seebeck coefficient is based on two basic rules: Firstly, the total inflow electric current is divided based on the current sharing principle of a parallel circuit, where $\frac{J_1}{\sigma_1}=\frac{J_2}{\sigma_2}$, and $J=J_1c_1+J_2c_2$. Through this relation, one can obtain

$$\begin{cases} J_1=\dfrac{\sigma_1}{\sigma_1c_1+\sigma_2c_2}J \\ J_2=\dfrac{\sigma_2}{\sigma_1c_1+\sigma_2c_2}J \end{cases} \tag{S15}$$

Secondly, the summation of Peltier heat released or absorbed by the two single sheets should be equal to the Peltier heat released or absorbed by the equivalent material: $JS_{eff}=J_1S_1c_1+J_2S_2c_2$. Substitute this into the expression of S_{eff}, one can obtain

$$S_{eff}=\frac{S_1\sigma_1c_1+S_2\sigma_2c_2}{\sigma_1c_1+\sigma_2c_2} \tag{S16}$$

Then, according to the relation between Seebeck coefficient and Thomson coefficient, we can get the equivalent Thomson coefficient as

$$\tau_{eff}=T\frac{dS_{eff}}{dT}=\frac{\sigma_1c_1}{\sigma_1c_1+\sigma_2c_2}T\frac{dS_1}{dT}+\frac{\sigma_2c_2}{\sigma_1c_1+\sigma_2c_2}T\frac{dS_2}{dT}=\frac{\tau_1\sigma_1c_1+\tau_2\sigma_2c_2}{\sigma_1c_1+\sigma_2c_2} \tag{S17}$$

Similarly, the equivalent electric conductivity and equivalent thermal conductivity can be derived as

$$\begin{cases} \sigma_{eff}=\sigma_1c_1+\sigma_2c_2 \\ \kappa_{eff}=\kappa_1c_1+\kappa_2c_2 \end{cases} \tag{S18}$$

Figure 3f in the main text shows that even with only a very thin copper layer deposited on the Bi_2Te_3 in channel 2, the electric current path can be significantly altered, where the majority of the electric current tends to flow through the copper due to its much higher electrical conductivity. As a result, the heat released via the Peltier effect at drain 1 is effectively prevented from being subsequently dragged away by the electric current from drain 1 to channel 2, because the difference of Seebeck coefficients at the interface has been significantly reduced. However, when the copper content becomes excessively high, a degradation in thermal splitting performance is observed. This can be attributed to the fact that, although the small effective Seebeck coefficient of channel 2 minimizes undesired Peltier pumping, the high thermal conductivity of copper significantly enhances passive heat diffusion between drains 2 and 3, undermining the routing effect. Therefore, an inherent trade-off exists between minimizing parasitic Peltier effects and limiting unwanted thermal conduction, which must be balanced through careful material selection in channel 2. Besides, despite the copper-volume dependence of the device, it is evident that a relatively broad optimal range exists for the copper proportion, confirming the robustness of our design.

Section S8: Method of calculating heat flux from temperature data

Whether using an infrared thermal camera in experiments or performing numerical calculations in theoretical studies, the raw data obtained only contains temperature measurements. However, the physical quantity of interest, the split ratio, is directly related to the heat flux. Therefore, determining the exact value of the heat flux from temperature raw data is of great importance for both theoretical analysis and experimental validation. This section presents the corresponding derivation method.

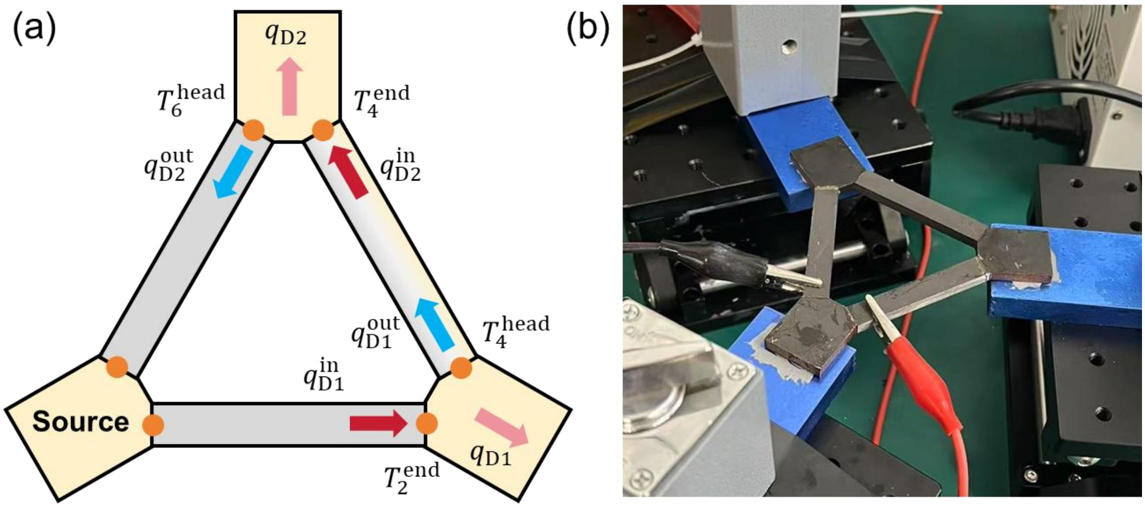

Figure S6. (a) The schematic of the heat energy routing path. (b) Photographs of the Experimental setup.

As stated above, the general solution of thermal diffusion governed by $\kappa\frac{d^2T}{dx^2}$-$J\tau\frac{dT}{dx}$+$\frac{J^2}{\sigma}$+h(T_0-T)=0 can be written as $T(x)$=Ce^{mx}+De^{nx}+T_0+u, where $m=\frac{\frac{J\tau}{\kappa}+\sqrt{\left(\frac{J\tau}{\kappa}\right)^2+\frac{4\mathrm{h}}{\kappa}}}{2}$, $n=\frac{\frac{J\tau}{\kappa}-\sqrt{\left(\frac{J\tau}{\kappa}\right)^2+\frac{4\mathrm{h}}{\kappa}}}{2}$, and $u=\frac{J^2}{\sigma\mathrm{h}}$ for clarity. Given the boundary condition $\begin{cases}T(0)=T^{\mathrm{head}}\\T(L)=T^{\mathrm{end}}\end{cases}$, the coefficients C and D can be derived as:

$$\begin{cases}C=\dfrac{T^{\mathrm{head}}e^{nL}\text{-}T^{\mathrm{end}}+(T_0+u)(1\text{-}e^{nL})}{e^{nL}\text{-}e^{mL}}\\[2ex]D=\dfrac{T^{\mathrm{head}}e^{mL}\text{-}T^{\mathrm{end}}+(T_0+u)(1\text{-}e^{mL})}{e^{mL}\text{-}e^{nL}}\end{cases}\tag{S19}$$

Based on Eq. S19 and substitute $T(x)$ into the formula q=-$\kappa\frac{dT}{dx}$+JST, we can obtain that for drain 1, $q_{\mathrm{D1}}^{\mathrm{in}}$=-$\kappa_{\mathrm{TE}}(C_2m_2e^{m_2L_2}+D_2n_2e^{n_2L_2})+JS_{\mathrm{TE}}T_2^{\mathrm{end}}$, $q_{\mathrm{D1}}^{\mathrm{out}}$=-$\kappa_{\mathrm{eff}}(C_4m_4+D_4n_4)+JS_{\mathrm{eff}}T_4^{\mathrm{head}}$. For drain 2, $q_{\mathrm{D2}}^{\mathrm{in}}$=-$\kappa_{\mathrm{eff}}(C_4m_4e^{m_4L_2}+D_4n_4e^{n_4L_2})+JS_{\mathrm{eff}}T_4^{\mathrm{end}}$, $q_{\mathrm{D2}}^{\mathrm{out}}$=-$\kappa_{\mathrm{TE}}(C_6m_6+D_6n_6)+JS_{\mathrm{TE}}T_6^{\mathrm{head}}$.

Therefore, the total heat fluxes absorbed by drain 1 and drain 2 are as follows:

$$\begin{cases}q_{\mathrm{D1}}=q_{\mathrm{D1}}^{\mathrm{in}}\text{-}q_{\mathrm{D1}}^{\mathrm{out}}=\text{-}\kappa_{\mathrm{TE}}(C_2m_2e^{m_2L_2}+D_2n_2e^{n_2L_2})+JS_{\mathrm{TE}}T_2^{\mathrm{end}}+\kappa_{\mathrm{eff}}(C_4m_4+D_4n_4)\text{-}JS_{\mathrm{eff}}T_4^{\mathrm{head}}\\q_{\mathrm{D2}}=q_{\mathrm{D2}}^{\mathrm{in}}\text{-}q_{\mathrm{D2}}^{\mathrm{out}}=\text{-}\kappa_{\mathrm{eff}}(C_4m_4e^{m_4L_2}+D_4n_4e^{n_4L_2})+JS_{\mathrm{eff}}T_4^{\mathrm{end}}+\kappa_{\mathrm{TE}}(C_6m_6+D_6n_6)\text{-}JS_{\mathrm{TE}}T_6^{\mathrm{head}}\end{cases}\tag{S20}$$

The positions of temperature and directions of flux are marked in Figure S6a, while the variables C_i, D_i, m_i, and n_i can be found in S3. To minimize random errors, three independent groups of experiments were conducted, with the experimental setup shown in Figure S6b, and corresponding data presented in Figure S7–S9. Following the calculation method described above, only six temperature values, namely, the initial and final temperatures of each of the three channels, are required from each thermograph, together with pre-set parameters, to determine the thermal split ratio under a given excitation current.

As can be observed from the thermographs, although the temperature field is asymmetrically distributed on the thermal router, the asymmetry appears relatively subtle. This is understandable: according to prior theoretical analysis, under the constraint of externally applied constant-temperature reservoirs as boundary conditions, only the Thomson effect can directly modify the temperature field distribution, whereas the Peltier effect functions more like a latent-heat conversion mechanism. This also explains why, from a thermodynamic perspective, the Peltier effect is reversible, whereas the Thomson effect is irreversible. By harnessing both effects in combination, the present thermal router achieves a decoupling of the temperature field and the heat flux, that is, pronounced asymmetric heat flux transport can be realized even when the temperature field asymmetry is not obvious.

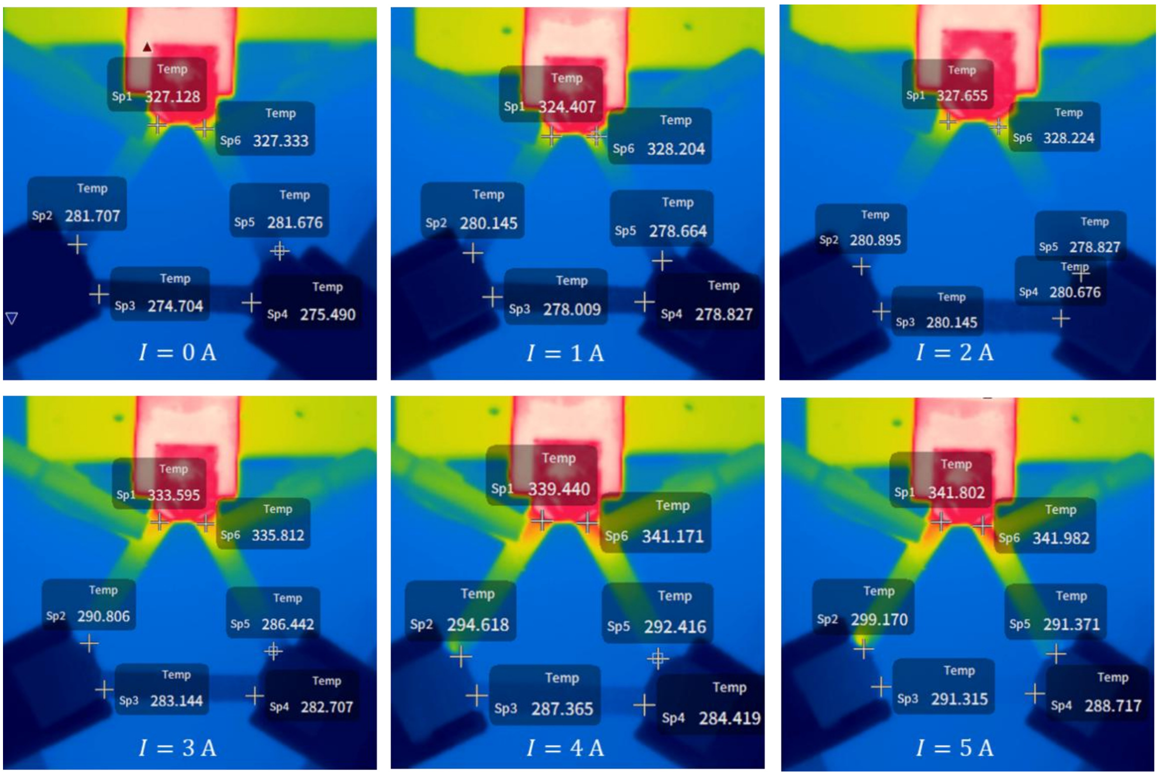

Figure S7. Raw temperature data with electric current ranging from 0 A to 5 A. Experiment group 1.

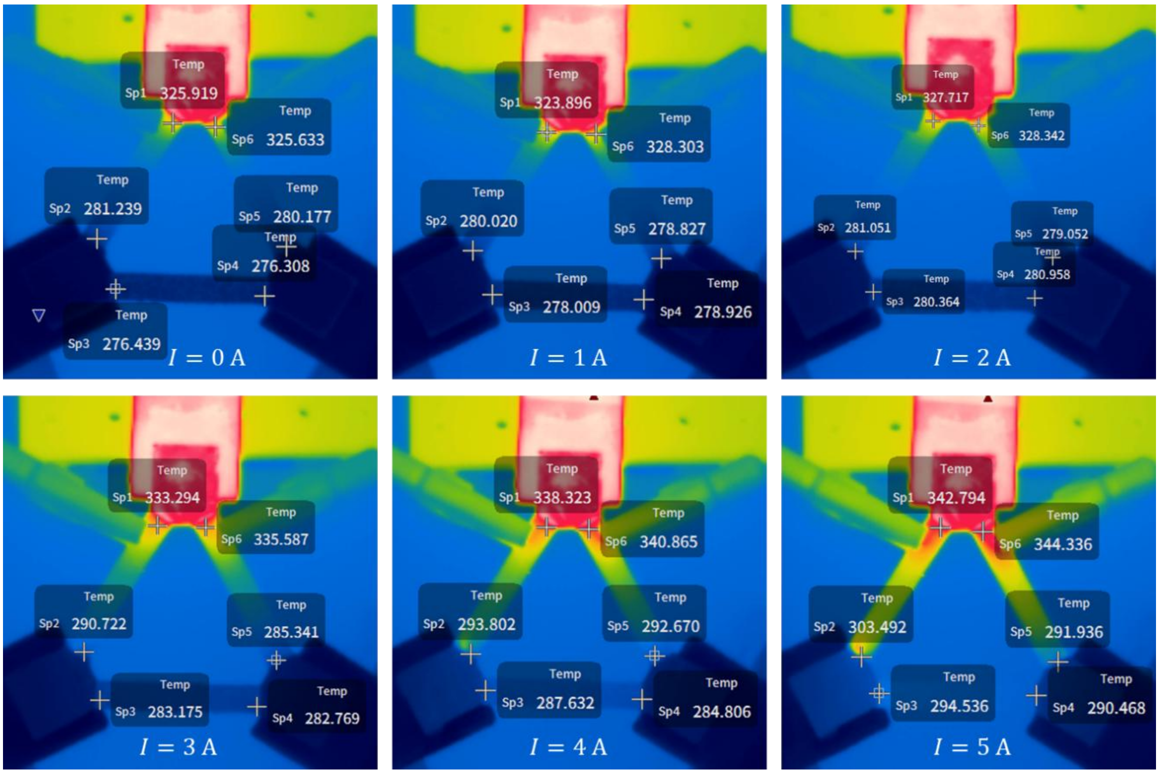

Figure S8. Raw temperature data with electric current ranging from 0 A to 5 A. Experiment group 2.

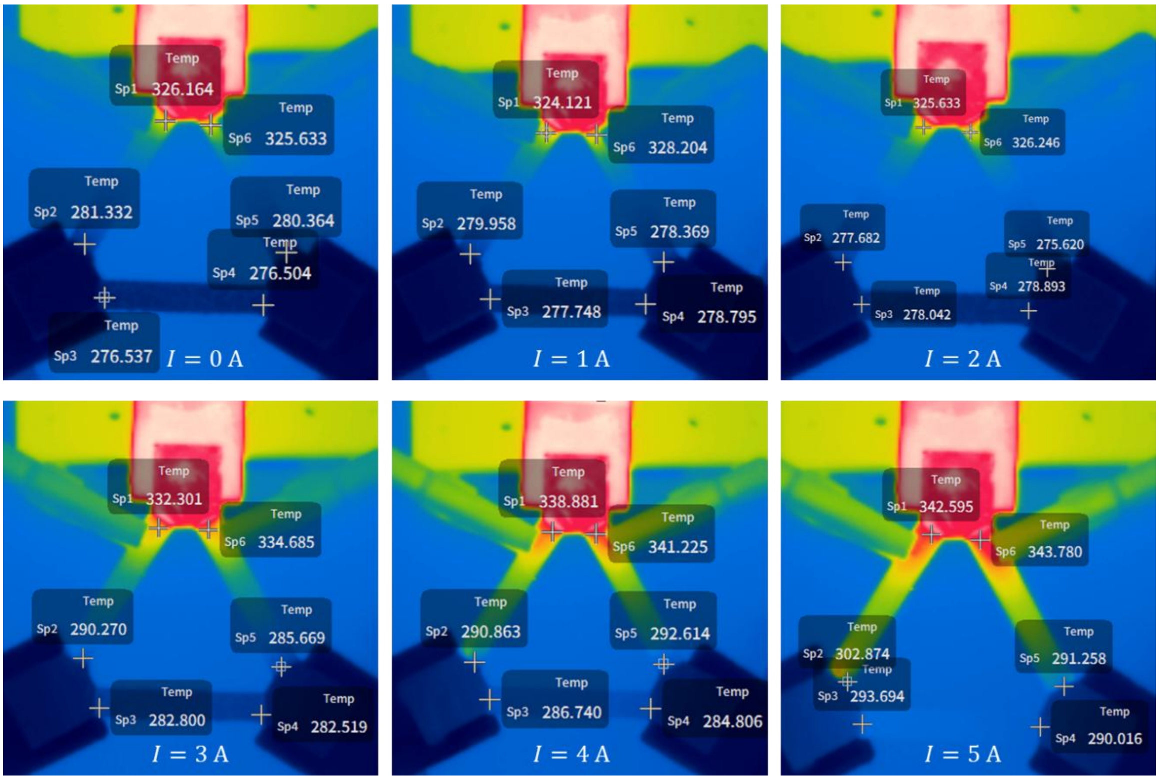

Figure S9. Raw temperature data with electric current ranging from 0 A to 5 A. Experiment group 3.

Section S9: Discussion of the discrepancy in split ratios between ideal and experimental cases

The substantially lower experimental ratio was due to two reasons. First, due to the low thermal conductivity of thermoelectric material, the energy loss through natural convection is unignorable. Second, our device is fabricated by connecting several sole material segments using specific glues, where the interfacial thermal resistance is unignorable. For these two reasons, the experimental split ratio is substantially lower than the theoretical one.

To evaluate the practical limitations of these two points, here we simulated their respective influence on the routing performance numerically, using the parameters achieved from experiment through fitting. According to our results, as can be seen in Figure S10, compared with the influence of interfacial thermal resistance, the performance degradation due to natural convection is more substantial. However, this is not a problem if the targeting application scenario is aerospace, where a vacuum condition is provided naturally. As far as the interfacial thermal resistance, the problem can be mediated by using more advanced fabricating technologies. Restricted by the experimental facilities, here we manually connecting the sample using specific glues, therefore causing this problem. To conclude, although the experimental split ratio is substantially lower than the theoretical one, it is a condition-restricted defect rather than an unsolvable obstacle.

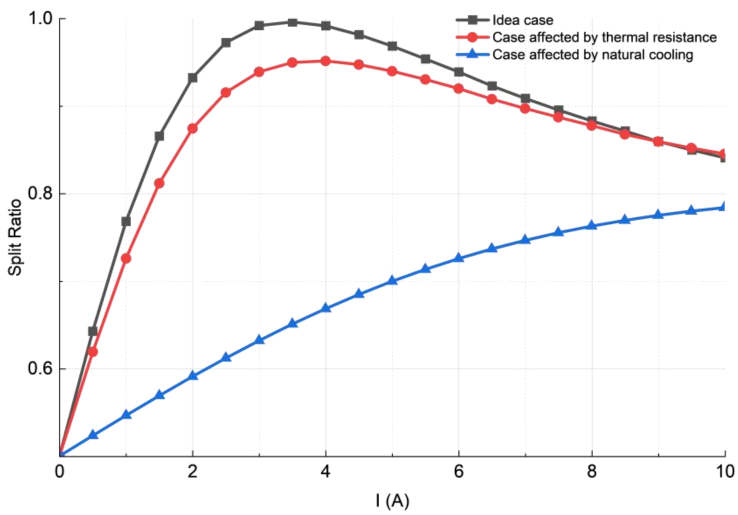

Figure S10 Quantitative analysis of the thermal routing performance affected by interfacial thermal resistance and air convection. Here a natural convection heat transfer coefficient h=15 W/(m^2·K) is assumed in the simulation.

Section S10: The dependence of thermal splitting performance on the router's geometrical size

Given that thermoelectric materials are typically brittle and costly, requiring careful handling during processing and assembly to avoid mechanical failure, the experimental model constructed in this study was intentionally large to facilitate operation and improve mechanical stability. Each individual TE slab has dimensions of 6 cm × 1 cm × 0.5 cm. Consequently, a relatively high driving current was necessary to operate the device effectively, with optimal performance observed at approximately 3 A. However, such a high current is impractical for integrated thermal management systems. Luckily, our analysis shows that the device's thermal routing performance is largely independent of its geometric scale. That is, when the device is uniformly scaled down, the separation ratio can still approach unity under ideal conditions. In contrast, the required driving current decreases linearly with the device size. For example, as illustrated in Figure S11, reducing the device dimensions to one-tenth of the original size results in a proportional reduction in the optimal operating current, from 3 A to approximately 300 mA. This trend confirms a linear scaling relationship.

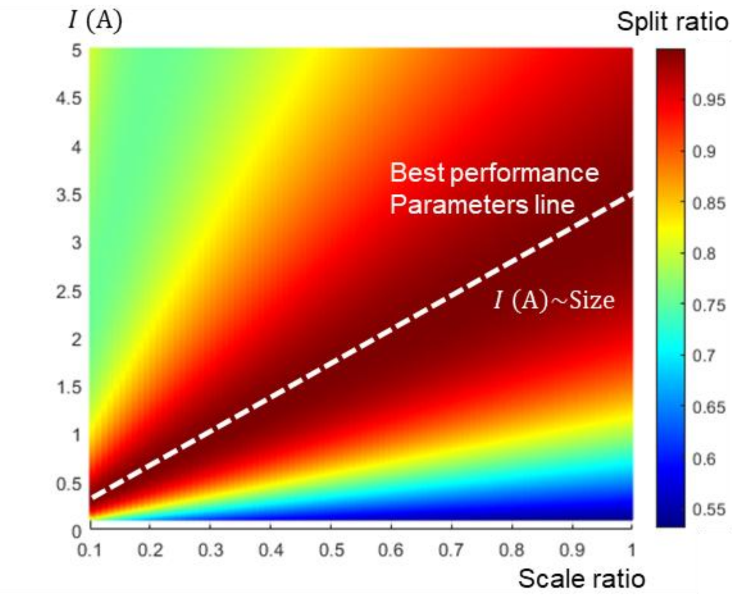

Figure S11. The dependence of split ratio on the geometric size and electric current ***I*.**

These findings indicate that the thermal routing performance of the device is not bound to a specific size. With the aid of precision microfabrication techniques, the device can be miniaturized to meet the thermal and electrical constraints of practical applications. However, this does not mean that the scaling effect of the structure is not subject to any limitations. To clarify this point, here we assume a scale ratio s, where s<1. Under uniform geometric scaling, the characteristic length and cross-sectional area scale as ($L_s=sL_0$) and ($A_s=s^2A_0$). According to our observation, the relative thermoelectric routing strength and Joule-heating contribution are governed by dimensionless parameters containing (JL/D), similar routing performance can be maintained when (JL/D) remains approximately constant. This property just resembles the Peclet number $Pe=\frac{vL}{D}$, a dimensionless number used to quantify the dominance of advection relative to diffusion. As a result, the uniform downscaling effect reduces the total driving current

(I_s=I_0*s<I_0) and total Joule power (I_s^2*R_s=$\frac{(J_sA_s)^2L_s}{\sigma A_s}$=$s^2\frac{J_0^2A_0L_0}{\sigma}$<$\frac{J_0^2A_0L_0}{\sigma}$), but it increases the operating current density (J_s=$\frac{I_s}{A_s}$=$\frac{J_0}{s}$>J_0) and volumetric Joule heating ($\frac{J_s^2}{\sigma}$=$\frac{1}{s^2}\frac{J_0^2}{\sigma}$>$\frac{J_0^2}{\sigma}$). Therefore, miniaturization is beneficial in terms of total current consumption, but cannot be extrapolated indefinitely. The lower size limit is set by factors such as allowable current density and local Joule heating, which should be a trade-off subject to practical application constraints.

Section S11: Experimental design, statistical analysis, and model parameters

Experimental design**:** The experiment was conducted in a laboratory environment with room temperature and atmospheric pressure. A tunable DC power supply, two temperature-controlled heat reservoirs, a thermal infrared camera (Fotric 628C), and test samples fabricated from a combination of Bi_2Te_3 and copper are involved in the measurement. The thermoelectric slab measured 6 cm×1 cm×0.5 cm, with Bi_2Te_3 selected as the material owing to its physical properties and commercial availability. The experimental device was assembled using three commercial thermoelectric strips (sintered Bi_2Te_3 powder), a copper sheet, three CNC-machined copper ports, and two industrial adhesives. The first adhesive (glue 1) was thermally and electrically conductive, while the second adhesive (glue 2) was thermally conductive but electrically insulating. Assembly proceeded as follows. One thermoelectric strip was bonded to a copper sheet of matching size to form channel 2. Copper ports were then attached to both ends of channel 2 with glue 1 under compression, ensuring strong thermal and electrical contact. The remaining two thermoelectric strips were bonded with glue 1 to form channels 1 and 3, connecting to the copper ports on the drain side. Finally, glue 2 was used to affix the last copper port to the ends of channels 1 and 3, providing thermal contact while maintaining electrical isolation. After assembly, the device was left at room temperature for over 24 hours to allow the adhesives to fully cure. To enable accurate infrared thermal imaging, the surface was coated uniformly with one layer of black graphite spray paint and air-dried, yielding an emissivity close to 1. With this preparation completed, the device was ready for platform integration and experimental testing. Three precision translation stages were arranged at 120° intervals and leveled to form the experimental platform. Liquid-circulating metal heads with constant temperatures were mounted on each stage to serve as the heat source and sinks. A thin layer of thermal grease was applied to all circulating head surfaces to enhance thermal contact. The assembled thermoelectric device was then positioned atop the platform, ensuring firm contact between the copper ports and the cooling heads, thereby establishing stable and uniform boundary conditions. Electrical excitation was applied by clamping two copper electrodes from the power supply onto the device, driving current counter-clockwise through the structure. The experiment aimed to validate the asymmetric temperature distribution and thermal-splitting behavior predicted by theoretical analysis and COMSOL simulations under steady-state conditions.

Statistical analysis: A thermal infrared camera was mounted above the setup with an optimized focal length to capture the device's surface temperature distribution. By varying the amplitude of the applied DC current, temperature fields under different operating conditions were recorded. All simulations were performed in COMSOL Multiphysics, while theoretical calculations were conducted in MATLAB using the parameters listed in the *Model Parameters* section. Details of the theoretical derivations and data processing methods are provided in the Supporting Information.

Model parameters: The three ports here were all made of copper, with thermal conductivity κ = 400 W·m^{-1}·K^{-1}, density ρ = 8,700 kg·m^{-3}, thermal capacity C_p = 385 J·kg^{-1}·K^{-1}, electric conductivity $\sigma = 5.7 \times 10^7$ S·m^{-1}, and Seebeck coefficient $S_{\mathrm{Cu}} = 1.7 \times 10^{-5}$ V·K^{-1}. The length, width and thickness of the channels are 6 cm, 1 cm, and 0.5 cm, respectively. They are made of Bi_2Te_3, whose parameters are set as: thermal conductivity κ = 1.7 W·m^{-1}K^{-1}, density ρ = 7,700 kg·m^{-3}, thermal capacity C_p = 154 J·kg^{-1}·K^{-1}, electric conductivity $\sigma = 7.2\times10^4$ S·m^{-1}, and a temperature-dependent Seebeck coefficient $S(T) = 9.8 \times 10^{-5}\log(T) - 3.5\times 10^{-4}$ V/K.